Materials Horizons

ROYAL SOCIETY OF CHEMISTRY

COMMUNICATION

View Article Online
View Journal

Cite this: DOI: 10.1039/d3mh01950k

Received 18th November 2023,
Accepted 24th June 2024

DOI: 10.1039/d3mh01950k

rsc.li/materials-horizons

Affective computing for human–machine interaction *via* a bionic organic memristor exhibiting selective *in situ* activation†

Bingjie Guo,‡[a] Xiaolong Zhong,‡[b] Zhe Yu,*[c] Zhilong He,[a] Shuzhi Liu,[a] Zhixin Wu,[b] Sixian Liu,[b] Yanbo Guo,[b] Weilin Chen,[b] Hongxiao Duan,[b] Jianmin Zeng,[b] Pingqi Gao,[c] Bin Zhang,[d] Qian Chen,[de] Haidong He,[e] Yu Chen *[d] and Gang Liu *[ab]

Affective computing, representing the forefront of human–machine interaction, is confronted with the pressing challenges of the execution speed and power consumption brought by the transmission of massive data. Herein, we introduce a bionic organic memristor inspired by the ligand-gated ion channels (LGICs) to facilitate near-sensor affective computing based on electroencephalography (EEG). It is constructed from a coordination polymer comprising Co ions and benzothiadiazole (Co–BTA), featuring multiple switching sites for redox reactions. Through advanced characterizations and theoretical calculations, we demonstrate that when subjected to a bias voltage, only the site where Co ions bind with N atoms from four BTA molecules becomes activated, while others remain inert. This remarkable phenomenon resembles the selective *in situ* activation of LGICs on the postsynaptic membrane for neural signal regulation. Consequently, the bionic organic memristor network exhibits outstanding reliability (200 000 cycles), exceptional integration level (2^{10} pixels), ultra-low energy consumption (4.05 pJ), and fast switching speed (94 ns). Moreover, the built near-sensor system based on it achieves emotion recognition with an accuracy exceeding 95%. This research substantively adds to the ambition of realizing empathetic interaction and presents an appealing bionic approach for the development of novel electronic devices.

New concepts

We report a bionic organic memristor network for near-sensor affective computing and high precision emotion recognition. Existing studies show that affective computing significantly enhances human–machine interaction (HMI) by gathering physiological electroencephalogram (EEG) signals, while its substantial data processing imposes considerable challenges on the execution speed and power consumption of the system. In this work, we purposely utilize a coordination polymer comprising Co ions and benzothiadiazole (Co–BTA) with multiple switching sites for *in situ* redox reactions, inspired by the selective *in situ* activation of ligand-gated ion channels, to construct a bionic organic memristor network. Our results show that the bionic organic memristor network based on the polymer exhibits excellent resistive switching performances, including reliability (200 000 cycles), exceptional integration level (2^{10} pixels), ultra-low energy consumption (1.08 pJ), and ultra-fast switching speed (25 ns). An implementation utilizing this bionic organic memristor network for EEG-based emotion recognition achieves high accuracy (>95%). This work provides an attractive bio-inspired method for the development of novel electronic devices and an application of energy-efficient near-sensor affective computing.

Introduction

Affective computing represents an emerging technological paradigm that empowers machines, particularly robots, with the capacity to recognize, interpret, and respond to human emotions.[1–4] This advancement holds significant implications across various domains;[5,6] in particular, the accuracy and harmony of human–machine interaction (HMI) will be significantly enhanced, as affective computing serves as a catalyst for liberating robots from preconceived notions. Presently, the predominant approach to implement affective computing is analyzing behavioral characteristics or physiological attributes gathered through sensors, such as natural language,[7] human postures,[8] facial expressions,[9] electroencephalogram (EEG) signals,[10] *etc.* Among these characteristic signals, EEG stands out as a real-time indicator of brain activity recorded from the scalp, allowing affective computing based on it to genuinely

[a] School of Chemistry and Chemical Engineering, Shanghai Jiao Tong University, Shanghai 200240, China. E-mail: gang.liu@sjtu.edu.cn
[b] Department of Micro/Nano Electronics, School of Electronic Information and Electrical Engineering, Shanghai Jiao Tong University, Shanghai 200240, China
[c] School of Materials, Sun Yat-Sen University, Guangzhou, Guangdong 510275, China
[d] School of Chemistry and Molecular Engineering, East China University of Science and Technology, Shanghai 200237, China
[e] Minhang Hospital, Fudan University, Shanghai 201199, China

† Electronic supplementary information (ESI) available: Fig. S1–S15 and Tables S1 and S2. See DOI: https://doi.org/10.1039/d3mh01950k

‡ These authors contributed equally to this work.

reflect individual emotional states without concealment. However, its substantial data processing imposes considerable challenges on the execution speed and power consumption of the system.

Memristors, emerging devices endowed with large-scale in-memory computing capabilities, offer a significant avenue for addressing the challenges encountered in EEG-based affective computing through near-sensor data processing.[11] This approach has proven effective in mitigating the complexities associated with the transmission of voluminous data in diverse intelligent analyses. For instance, Wei D. Lu's research group and Heejun Yang's research group have employed the Pd/WO_x/Au memristor network and Au/SnS/Cr memristor network, respectively, to achieve fast and low-power execution of hand-written character recognition tasks.[12,13] Additionally, the team led by Ming Liu and Qi Liu integrated a Pt/Ti/Nb_2O_{5-x}/Pt memristor network with sensors to build a multimode-fused spiking neuron capable of recognizing pressure and temperature by near-sensors.[14] It is a regret that the aforementioned memristors are constructed from rigid inorganic materials, creating an inherent chasm in mechanical properties separating them and the flexible devices employed for EEG signal collection. In contrast, organic memristors with the characteristic of intrinsic flexibility are more suitable for seamless integration with flexible sensors, facilitating the development of near-sensor EEG-based affective computing.[15]

With the data explosion in the big data era, memristors are limited in their ability to process large amounts of data of near-sensor EEG-based affective computing. As the primary inspiration, the synapse is renowned for its ability to transmit neural signals in a high-throughput manner, which is conferred by the selective *in situ* activation of ligand-gated ion channels (LGICs) located on the postsynaptic membrane, as elucidated in Scheme 1a. After binding to neurotransmitters released from presynaptic neurons, LGICs open *in situ* to allow free ions within the synaptic gap to enter the postsynaptic neuron, accompanied by the generation of action potentials on the cell membrane. Different from other ion channels, such as mechanically-gated ion channels present on the mechano-receptor,[16] only a portion of the LGICs that can form chemical coordination with neurotransmitters are selectively opened uncontrollably. Recently, it has been widely reported that bionic organic memristors exhibit impressive performance attributes.[17] These advancements are due to their utilization of organic semiconductor materials, which offer distinct advantages in molecular design, synthesis methodologies, and large-scale production.[18,19] It provides a feasible technical route to solving the dilemma of EEG-based affective computing, that is, to develop a bionic organic memristor grounded in the distinctive operational principle of LGICs.

In this study, we have developed a bionic organic memristor that mimics LGICs by choosing a coordination polymer composed of cobalt ions and benzothiadiazole (Co–BTA) as an active material (Scheme 1b). Because substantial electron delocalization occurs as the hybridization of π–d conjugation between inorganic metals and the organic ligand,[20] the Co–BTA film possesses abundant Co–N coordination bonds to serve as active sites for resistive switching through *in situ* redox transformation. Meanwhile, there

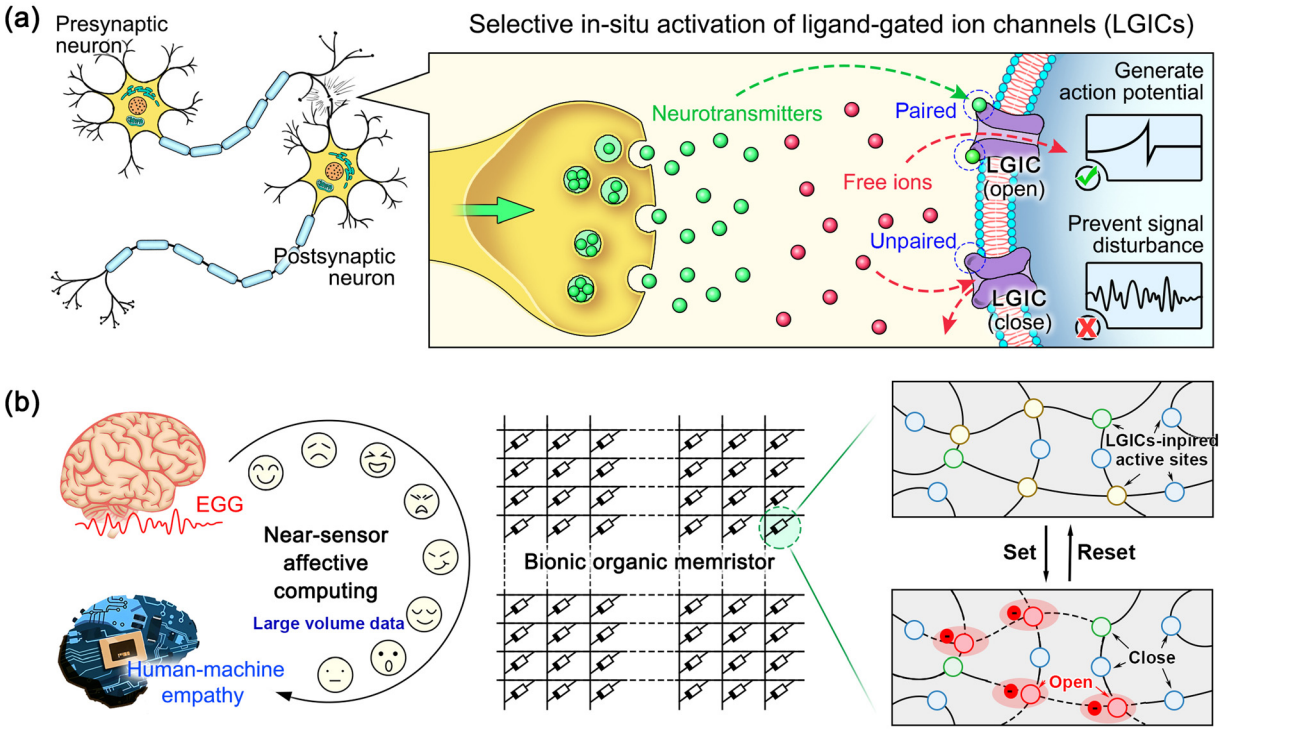

Scheme 1 (a) Schematic illustration of LGICs transmitting neural signals in a high-throughput manner through selective *in situ* activation. (b) Application of the bionic organic memristor inspired by LGICs in EGG-based affective computing and its mechanism of resistive switching.

are differences in the number of BTA molecules that provide N atoms for Co ions in these sites, resulting in a significant dispersion of their highest occupied molecular orbitals (HOMOs) under the steric hindrance effect with different strengths. It lays the foundation for selective *in situ* activation of our bionic organic memristor, which has been verified by various characterization analyzes and theoretical calculations. Therefore, the bionic organic memristor network based on Co–BTA exhibits excellent resistive switching characteristics, including outstanding reliability (200 000 cycles), high integration level (2^{10} pixels), ultra-low energy consumption (4.05 pJ), and fast switching speed (94 ns). Finally, our bionic organic memristor network was used as a near-sensor system to perform the task of EEG-based emotional computing, and the results showed that it can complete complex emotion recognition with an accuracy of 95%. This research opens up new possibilities for EEG-based affective computing and provides valuable insights for the advancement of near-sensor systems in HIM.

Results and discussion

In Fig. 1a, it shows a potential chemical structure of Co–BTA with multiple LGIC-like active sites. As a result of that discrepancy of the number of BTA molecules that provide binding N atoms for Co ions among these sites (highlighted by blue, green, and orange), their activation energies must be different, laying the foundation for selective *in situ* resistive switching. We employed a solid–liquid interfacial assembly method to synthesize the continuous Co–BTA film by dripping the mixed solution of $CoCl_2{\cdot}6H_2O$ and BTA·4HCl into ammonia on the surface of indium tin oxide (ITO). It can quickly self-assemble to form the desired coordination polymer, and this self-assembled growth involves three reactions: the adsorption of precursors, the organization of polar groups, and the occurrence of coordination effects. More details about the preparation process are included in the Experimental section and Fig. S1 of the ESI.† The molecular structure of the synthesized Co–BTA film is confirmed by Fourier transform infrared spectroscopy (FTIR). As seen in Fig. 1b, the main absorption peaks of 1315, 1532, 1099, and 3196 cm^{-1} are assigned to the stretching vibrations of C–N, C=C, C–C, and N–H bonds in the organic component of BTA, respectively. Notably, there is an absorption peak of C=N at 1625 cm^{-1}, which is a double-bond character of a partial C–N bond produced by the conjugation effect between metal cations and organic ligands, so that the coexistence of C–N and C=N bonds demonstrates the formation of coordination between the cobalt ion and BTA molecules.[21,22] Thanks to a controlled preparation method, the Co–BTA can be made into a large-area continuous film with high-quality flexibility (Fig. S2 of the ESI†). In addition, this liquid–solid interface method can adjust the film thickness by changing the number of repeated cycles of processing, as shown in Fig. S3 of the ESI† where the color of the film gradually deepens with the number of experiments from 1 to 6 times.

The excellent processing characteristic of Co–BTA film lays the material foundation for the development of high-performance devices, so a bionic organic memristor with the structure of Au/Co–BTA/indium tin oxide (ITO) was successfully manufactured by us. As shown in Fig. 1c and d, it can be found that its active layer of Co–BTA exhibits extremely high uniformity, such as a thickness of about 100 nm tested by scanning electron microscopy (SEM) and a roughness of less than 4 nm tested by atomic force microscopy (AFM). Furthermore, the ITO bottom electrode and Au top electrode of the bionic organic memristor were transformed into a crossbar structure by magnetron sputtering, thereby expanding the device into a highly

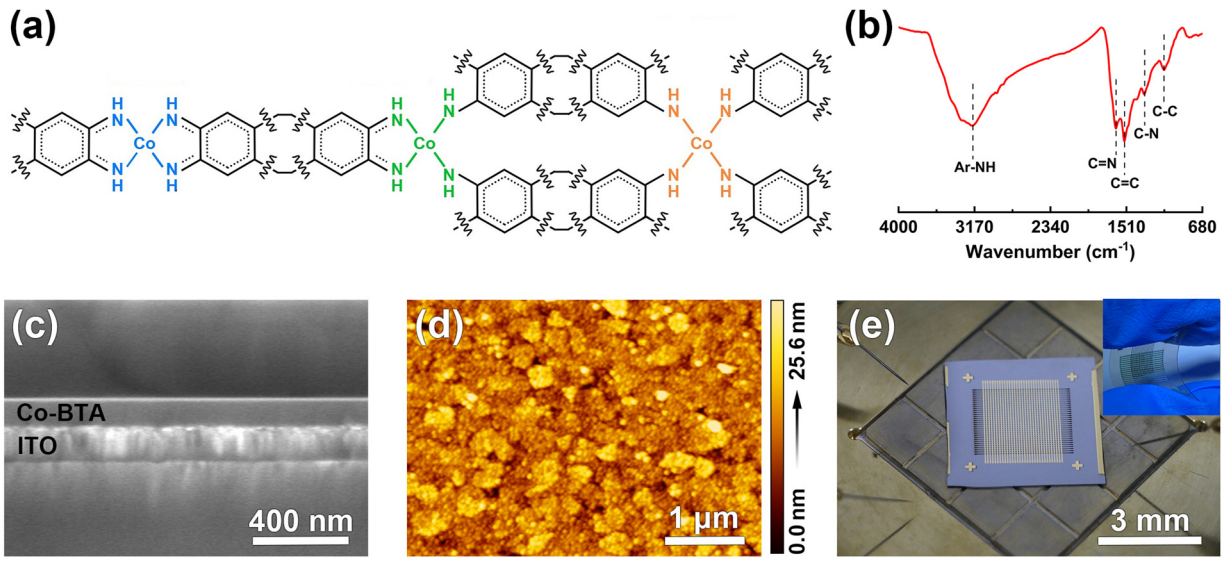

Fig. 1 (a) Potential chemical structure of the Co–BTA molecule. (b) FTIR spectra of the Co–BTA film. (c) SEM image of the Co–BTA film on the cross-sectional view. (d) AFM image of the surface morphology of the Co–BTA film. (e) Photograph of the bionic organic memristor network with the structure of Au/Co–BTA/ITO. The inset is a digital image of the flexible bionic organic memristor network under bent conditions.

integrated memristor network with 32 × 32 pixels (Fig. 1e), whose linewidth is 150 μm as shown in Fig. S4 of the ESI.† The intrinsic flexibility allows it to be bent substantially to match the mechanical properties of flexible EEG electrodes (the inset of Fig. 1e). Please note that SiO_2/Si was selected as the substrate for fabricating the memristor network, so it should be ultrasonically cleaned with deionized water, ethanol, and acetone in sequence before use, and each cleaning lasts for 30 minutes.

The current–voltage curves of our bionic organic memristor are recorded in Fig. 2a, and it shows that the memristor can switch from a high resistance state (HRS) to a low resistance state (LRS) at the voltage of 1.5 V (set voltage, V_s), exhibiting a sudden 20-fold increase in current. When applying a reverse voltage up to −0.75 V (reset voltage, V_r), the device will return to the HRS and remain stable for a long time. Repeating the above operation for 600 times, there is no significant change in the switching characteristics of our memristor, which can be demonstrated from the statistical results with V_s of 1.5 ± 0.50 V, V_r of −0.75 ± 0.25 V, HRS value of 3045.4 ± 1561.1 Ω, and LRS value of 190.4 ± 86.8 Ω (Fig. S5, the ESI†). Our bionic organic memristor also exhibits a stable non-volatile time retention (>10 000 s) and an ultra-low energy consumption for switching (4.05 pJ), as shown in Fig. 2b and c. Note that depending on the experimental setups, *e.g.* metal probes, cablings, measuring systems, *etc.*, the transient current responses of memristor devices may or may not show initial spikes upon the application of voltage stresses.[23–29] In order to comprehensively reflect the responding rate of our memristor, we define the switching speed as the time interval between when the stressing voltage starts to apply and when the current response reaches its maximum. As depicted in Fig. 2c, the present organic memristor shows a fast switching speed of 94 ns. Meanwhile, we tested the effect of bending on the performance of the memristor based on Co–BTA (Fig. S6 of the ESI†). During 100 bending

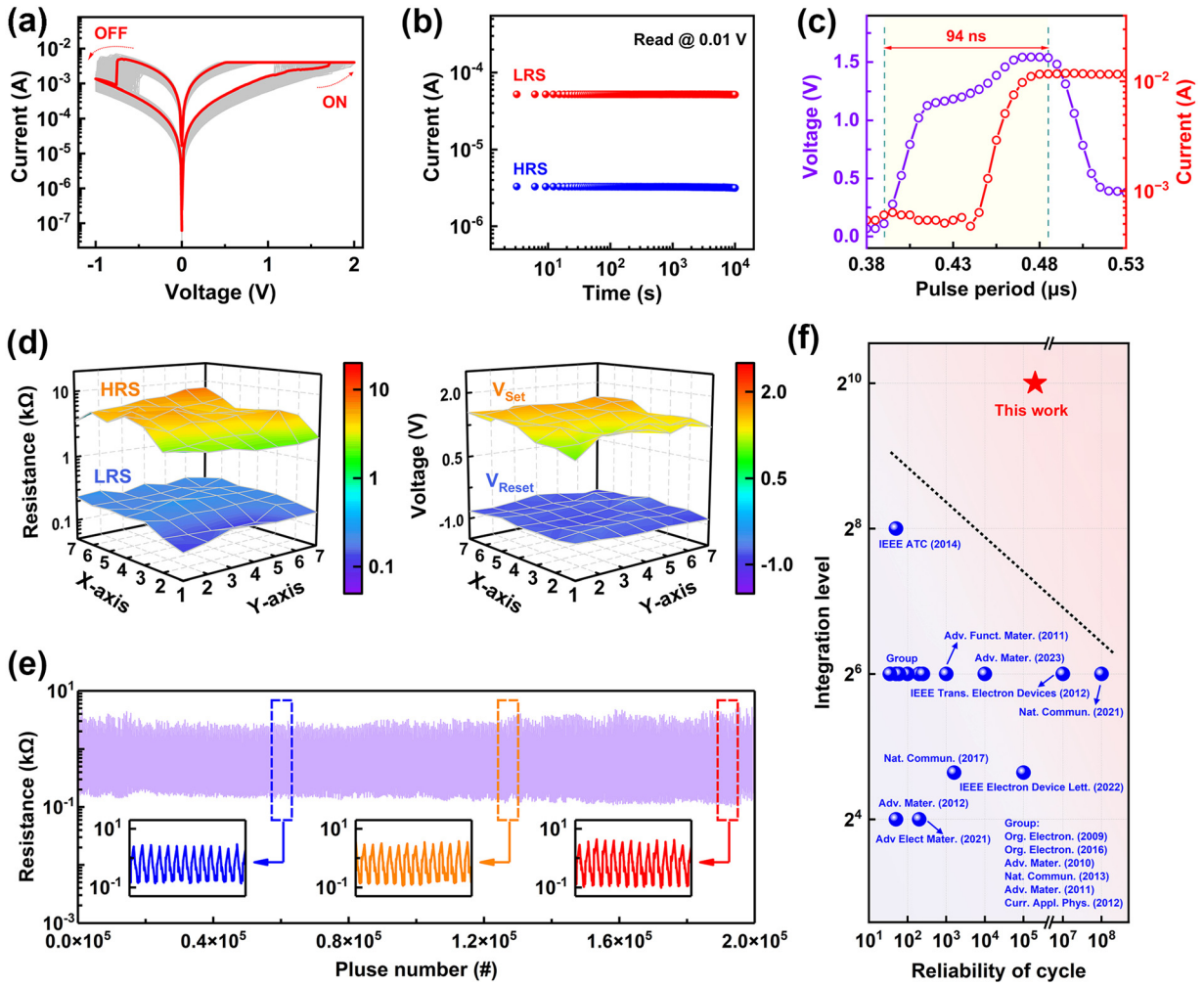

Fig. 2 (a) Typical current–voltage (I–V) characteristics cycles of a bionic organic memristor based on Co–BTA. (b) Retention performance test of the device at the HRS and LRS. (c) Immediate current response (red) of the device under the stimulation of pulsed voltage (purple). The current limitation is 1×10^{-2} A. (d) The three-dimensional color-map of HRS/LRS value (left) and V_s/V_r distribution (right) of the memristor network. The value of each pixel is the statistical result of 50 I–V curve tests. (e) The endurance test of the device under 200 000 pulses. The inner graph is enlarged curves within the box area. (f) Performance comparison (reliability of the cycle, and integration level) of our bionic organic memristor with other state-of-the-art organic memristors.

cycles with a bending radius of 1.83 cm, the average fluctuation of HRS/LRS values and switching voltages is lower than 6.75%, which means that the prepared bionic organic memristor can match a variety of wearable flexible sensors including EEG electrodes. To fully elaborate the reliability, we have tested the device-to-device (D2D) reliability and cycle-to-cycle (C2C) endurance of the Co–BTA organic memristor. The 49 pixels in memristor network were selected for D2D testing (Fig. S7 of the ESI†), and its statistical analyses are recorded in Fig. 2d, showing that the average fluctuation of the switching voltages is only 9.48%, yet that of the HRS/LRS resistance ratios reaches 28.7%. Nevertheless, the ON/OFF ratios are maintained for larger than 10 for all devices, which can be reliably distinguished by external CMOS read circuits. As described in the Experimental section and Fig. 2e, the Co–BTA memristor exhibits promising endurance performance, with the device resistances and ON/OFF ratios only varying for 3.77% during 200 000 continuous operating steps.[30] All these figures of merits make the reliability of our biomimetic memristor significantly superior to other reported organic memristors (Fig. 2f).[31–45]

Before verifying the bionic resistive switching behavior of the Co–BTA film, it is necessary to confirm the types of active sites formed by Co ions in it, so we employ a variety of characterization techniques and advanced theoretical calculations. From the test results of X-ray photoelectron spectroscopy (XPS) in Fig. S8 of the ESI,† it can be found that the composition of the film mainly consists of Co, N, and C elements, and the deconvolution of the N 1s peaks at 399.0 eV and 401.5 eV reveal the presence of anilinic amine (–N–H–) and quinoid imine (–N=) groups, respectively. These peaks indicate the formation of conjugation and electronic delocalization within the π–d conjugated structure. The binding energy of the Co $2p_{3/2}$ peak and the accompanying satellite peak is 781.9 eV and 787.1 eV, respectively, consistent with Co^{2+} compounds rather than Co^{3+} compounds.[30,46,47] Based on these observations, we believe that the N atoms coordinated with Co ions can originate from 2, 3, or 4 BTA molecules (Z = 2, 3, or 4), which means that there are three different types of active sites in the Co–BTA. It is further characterized and confirmed by density functional theory (DFT). In the active sites with Z of 2, or 3, the Co ions and their coordinated BTA molecules are in the coplanar state, while the site with Z of 4 is like butterflies flapping their wings in space, *i.e.* four non-coplanar coordination molecules, as shown in Fig. 3a–c. The more structural images of the three

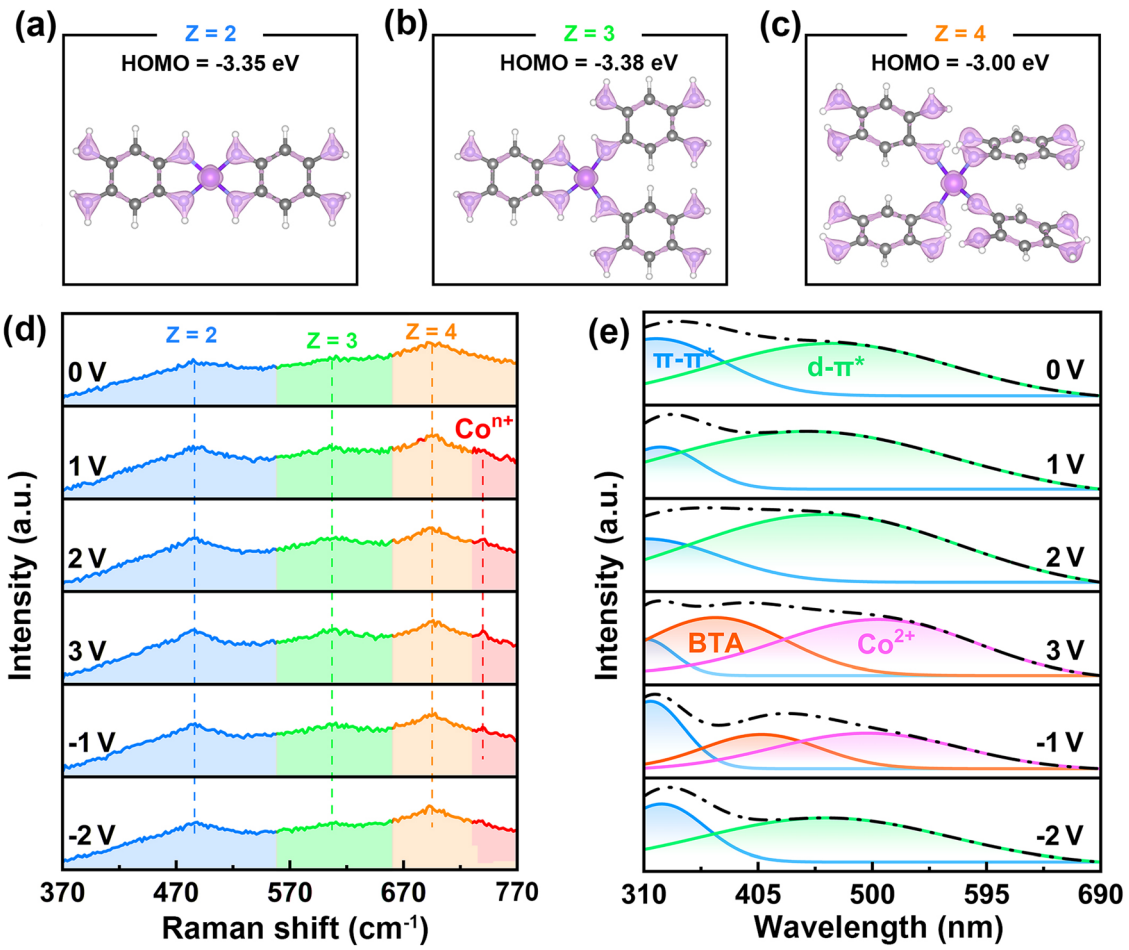

Fig. 3 (a)–(c) Molecular structures of active sites in Co–BTA films. They are the calculation results of DFT. *In situ* measurement of the (d) Raman spectrum and (e) UV-Vis spectrum of the electrochemical device based on Co–BTA stimulated by different bias voltages.

active sites under different visual angles can be found in Fig. S9 of the ESI,† and their structural parameters are detailed in Tables S1 and S2 of the ESI.† All tests show that the Co–BTA film has three types of active sites, laying a data foundation for analyzing its bionic resistive switching behavior.

According to the electrostatic potential calculated by DFT, there is a significant electron-deficient effect in the Co–N coordination bond across all active sites, and their energies of the highest occupied molecular orbit (HOMO) respectively are −3.35 eV (Z = 2), −3.38 eV (Z = 3), and −3.00 eV (Z = 4). This suggests that the resistive switching of the Co–BTA film is achieved through the redox transition of the Co–N bond at the active sites, where the active site with Z of 4 is the easiest among the three to lose electrons for transition under the bias voltage. Considering that the DFT calculation is ideal, an electrochemical Pt-tip/Co–BTA/ITO device (Fig. S11 of the ESI†) is designed for *in situ* characterization of Raman spectroscopy to explore the microscopic changes of an actual sample during resistance switching. The results of Raman spectral analysis of the film under different bias voltages are recorded in Fig. 3d. As we all know, the infrared absorption peak of chemical bonds with similar structures red-shifts with the increase of the steric hindrance. From the chemical structures of the three active sites, the steric hindrance of the site with Z of 2 and that of the site with Z of 4 is the smallest and largest, respectively, so the three absorption peaks of the Co–N bond (486.7 cm^{-1}, 603.2 cm^{-1}, and 694.4 cm^{-1}) from left to right in the infrared spectrum respectively belong to the active sites with Z of 2, 3, and 4 under the bias voltage of 0 V. When the Co–BTA film is subjected to the bias voltages of 1 V, 2 V, and 3 V, there is a new absorption peak (740 cm^{-1}) appearing on the leftmost absorption peak of the Co–N bond, which is attributed to the disconnection of the Co–N bond and the oxidation of Co ions in the active site with Z of 4. When applying the bias voltage of −1 V, and −2 V, the chemical environment of this active site returns to the original state with the gradual disappearance of the new peak. Importantly, the absorption peaks of other active sites (Z = 2, and 3) remain unchanged during this reversible reaction.

A similar phenomenon induced by chemical state transitions also occurs in the test of in-site ultraviolet-visible (UV-vis) spectroscopy. Initially, there are two main peaks at the wavelength of 320 nm (blue part) and 465 nm (green part) in Fig. 3e, which is influenced by the π–π* jumping of the conjugate structure and the d–π* metal-to-ligand charge transfer. The corroborative evidence for this part is described in Fig. S12 of the ESI,† including the UV-vis spectra of the individual components and their analyses. During oxidation under positive voltage, these two peaks gradually differentiate due to the destruction of the d–π conjugated structure of Co–N–C, yet the differentiated peaks recombine under a reverse voltage, indicating the restoration of the structure to its original state. These results can prove that our sample has a unique selective *in situ* redox transition for resistive switching, which is similar to the selective *in situ* activation of LGICs. Specifically, the active sites with Z of 2, 3, and 4 in the Co–BTA film can all be *in situ* activated through redox reactions, where the activation energy of the site with Z of 4 is the lowest, becoming the only one that is selectively *in situ* active under the stimulation of small voltage. This behavior is exactly the same as that of LGICs on

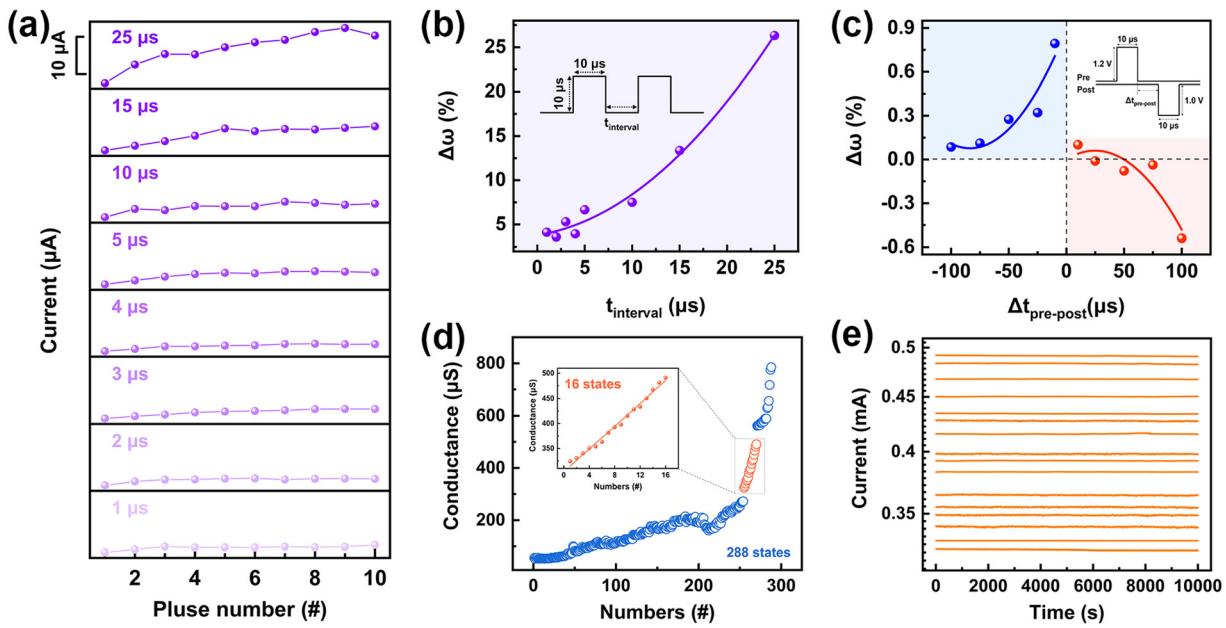

Fig. 4 (a) Changes of the current of the bionic organic memristor during long-term promotion. The amplitudes and widths of the applied voltage pulse are 0.8 V and 10 μs, respectively. (b) SRDP and (c) STDP characteristic tests of the bionic organic memristor based artificial synapse. (d) The 288 continuous conductance states of the device. The inset is 16 linear conductance states between 0.32 mA and 0.49 mA. (e) Retention performance test of 16 linear conductance states.

the postsynaptic membrane, which is enough to show that bionic molecular design is a potential strategy for improving device performance.

In order to show the potential for affective computing, emotion recognition is chosen as the application demonstration of our biomimetic organic memristor network, but before that, we have tested the computing capabilities of the bionic organic memristor as a neuromorphic device, including spike rate dependent plasticity (SRDP), spike timing dependent plasticity (STDP), and multiple conductance state regulation. In the SRDP tests, ten consecutive pulses of 10 μs with 0.9 V were used to stimulate the device, and the pulse frequency was altered by adjusting the interval time (25 μs, 15 μs, 10 μs, 5 μs, 4 μs, 3 μs, 2 μs, and 1 μs) between pulses to observe its impact on the synaptic conductance. The raw data tested on the device and the normalized results are exhibited in Fig. S13 of the ESI† and Fig. 4a, respectively. The synaptic conductance difference ($\Delta\omega$) is calculated by subtracting the 1st pulse conductance from the 10th pulse conductance. It can be found that the response current of the device increases with the increase of the stimulation pulse number and interval time, exhibiting a synaptic feature-related enhancement mechanism for the conductance dependence of time intervals (Fig. 4b). Fig. 4c depicts the STDP characteristics of the present Co–BTA memristor, with the changes of device conductance presented in the second and fourth quadrants of the plot. Note that although the Hebbian rule[48] describes four types of learning behaviors of biological nerve systems, it does not mean that all memristive synapses working on various switching and carrier transport mechanisms have to obey these traces exactly. Herein, the selective *in situ* activation and time-dependent oxidation of the $Z = 4$ redox center accounts for the unique memristive switching behaviors of the Co–BTA memristor devices, leading to anomalous STDP curves that cannot be fitted by any of the existing learning models of the biological Hebbian rule. Nevertheless, this new STDP curve may offer potential possibility to widen the circuit functionality of artificial memristive synapses. On the other hand, when a voltage from −0.4 V to 0.02 V is applied in the step of 0.02 V, as shown in Fig. S14 of the ESI,† the device is reset from HRS to LRS with the continuous current

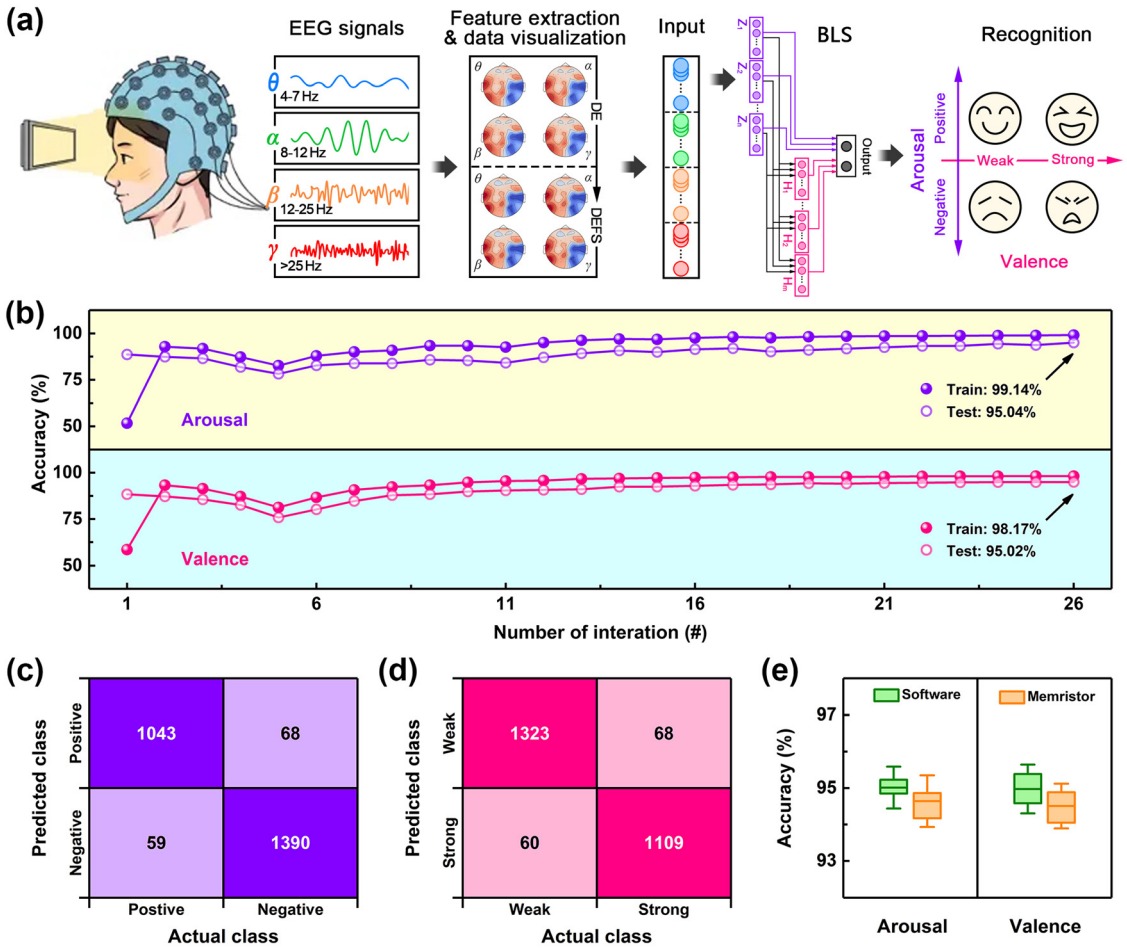

Fig. 5 (a) Schematic illustration of a near-sensing system built on a bionic organic memristor. It can perform EEG-based affective computing, benefiting from a bionic organic memristor network that emulates the intelligent algorithm of the broad learning system. (b) The identification accuracy of the arousal (top) and valence (bottom) dimensions with increasing interactions. Confusion matrix of (c) the arousal and (d) valence dimensions. (e) Accuracy comparison of the software-trained model and memristor-trained model on the arousal and valence dimensions.

variation, showing an ability for multiple conductance state regulation. It has a total of 288 continuous and adjustable conductance states (Fig. 4d), of which 16 conductance states between 0.32 mA and 0.49 mA were used to regulate the weights for emotion recognition due to their good linear change and time stability ($>10^4$ s, Fig. 4e).

Fig. 5a describes the working principle of the near-sensing system, which performs EEG-based affective computing by using the fabricated bionic organic memristor network to simulate a broad learning system (BLS). As a very popular artificial intelligence algorithm for processing EEG signals, BLS has the characteristics of real-time processing, low time complexity, and few-shot learning, so that its requirements for computing power and storage capacity of hardware are much lower than traditional deep learning models.[49–51] Our system is evaluated to recognize four target-emotions, that is happiness, excitement, sadness, and anger, which are divided into two categories of arousal dimension (ranging from negative to positive) and valence dimension (ranging from weak to strong). The detailed affective computing process is described in the Experimental section. After 26 times of iterative training (Fig. 5b), the system achieves exceptional recognition accuracy rates of 95.04% for arousal and 95.02% for valence dimensions on the testing datasets, which means the built system based on a bionic organic memristor can successfully achieve high-accuracy emotion recognition through affective computing. The confusion matrices for the arousal and valence emotional dimensions are presented in Fig. 5c and d, respectively. Interestingly, the number and distribution of samples with identification errors in the confusion matrices are very close (arousal: 59, and 68; valence: 60, and 68), which prompted us to conduct simulation on computer software. Fig. 5e shows the recognition results of the software-execution (arousal: 94.97% ± 0.61%; valence: 95.01% ± 0.71%), which is almost the same as that of the memristor-based hardware system, and their weights of the output layer closely follow a linear narrow distribution ranging from 0.002 to −0.002 (Fig. S15 of the ESI†). It reveals that there is a strong linear mapping between the software-trained weights and the linear conductance of our bionic organic memristor, allowing the emotion recognition system built on it to demonstrate the unique ability to realize high-precision affective computing, which is expected to become an important component in the next-generation HMI technology.

Conclusions

To summarize, we were inspired by the working principle of LGICs to develop a bionic organic memristor with Co–BTA as the active material, which exhibits outstanding reliability, high integration level, ultra-low energy consumption, and ultra-fast switching speed. Relying on a variety of *in situ* characterizations and advanced theoretical calculations, it is explained that these excellent resistive switching properties originate from a unique selective *in situ* activation of redox sites in Co–BTA films. Among the sites, only the one with Z of 4 is reversibly activated under bias voltage, while other sites (Z = 2, or 3) remained stable. This is very similar to how LGICs transmit neural signals through selective opening and closing to regulate the number of free ions entering the postsynaptic neuron. Moreover, our bionic organic memristor possesses the characteristics of a neuromorphic device, including SRDP, STDP, and 288 continuous conductance states, which lays the foundation for near-sensor affective computing based on EEG. As we expected, the built intelligent system can recognize the emotions of happiness, excitement, sadness, and anger with an accuracy of over 95% by simulating the BLS algorithm. This work opens up a new avenue for the development of an organic memristor, including the potential bionic molecular designs and prospective affective computing applications.

Experimental

Synthesis of Co–BTA film

The Co–BTA films were prepared on commercial ITO glass substrates by using the liquid–solid interface method. Firstly, $CoCl_2{\cdot}6H_2O$ (47.6 mg, Sinopharm) and BTA·4HCl (56.8 mg, Bide Pharmatech) powders were dispersed in 1000 μL of deionized water and then ultrasonicated at 100 Hz for 10 min to obtain a completely dissolved solution (hybrid solution). ITO glass substrates were ultrasonicated in deionized water, ethanol, and acetone for 30 min, respectively. After that, the treated and cleaned substrates were placed in an undisturbed and smooth fume cupboard, followed by which 200 μL ammonia was added to form a liquid–solid interface. Subsequently, a mixed solution (20 μL) was carefully dropped onto the ammonia and then left for 3 hours at room temperature to remove the solution and obtain Co–BTA film. Finally, the film was washed with deionized water, ethanol, and acetone, respectively. The process described above constituted one cycle of liquid–solid interface-assisted growth of the Co–BTA film. The film thickness can be adjusted by repeating several synthetic cycles.

Characterization of Co–BTA film

Transmission electron microscopy (TEM, Talos F200X G2) was used to study the nanostructure of Co–BTA film by directly growing it on copper wire operated at 200 kV. Scanning electron microscopy (SEM, JSM-7800F) operated at 10 kV was performed to study the microstructure of the Co–BTA film. Atomic force microscopy (AFM, MFP-3D) measurements were conducted in tapping mode to determine the thickness and roughness of the Co–BTA film. FTIR spectra were obtained by a microscopic infrared spectrometer (iN10 MX) with nanogram-level detection sensitivity. X-ray photoelectron spectroscopy (XPS, AXIS UltraDLD) was carried out using Al Kα X-rays as the excitation source to verify the elemental composition and chemical valence of Co–BTA. A confocal microscopy Raman spectrometer (Raman, Renishaw inVia Qontor) with a laser wavelength at 532 nm was used to clarify the molecular structure. Ultraviolet and visible spectrophotometer (UV-vis, EV300) was employed to

study the film structure on high transmittance conductive ITO substrates.

Fabrication and characterization of a bionic organic memristor based on Co–BTA

The electrical performance of the Co–BTA devices was analyzed in the configuration of Au/Co–BTA/ITO in a 32 × 32 crossbar array with an electrode linewidth of 150 μm. Firstly, after ultrasonication in deionized water, ethanol, and acetone for 30 min, the SiO_2/Si substrate was dried using a nitrogen gun. Following this, a patterned mask with 32 rectangles (150 μm width, 350 μm separation, and 2 cm length) was used to mask the SiO_2/Si substrate. The bottom ITO electrode was then patterned on the SiO_2/Si substrate through magnetron sputtering at 0.7 Pa for 30 min. The Co–BTA film, serving as the active material, was synthesized *via* the liquid–solid interface method. Finally, the top electrode Au was deposited onto the Co–BTA film through magnetron sputtering at 1.3 Pa for 30 min, using the same mask after rotating 90 degrees. This process resulted in the formation of the Au/Co–BTA/ITO device in a 32 × 32 crossbar structure. All electrical measurements were conducted using a Keithley 4200 semiconductor parameter analyzer. Current–voltage (*I–V*) curves of the Co–BTA memristor were recorded in a dc voltage sweep node, by varying the applied voltages from 0 V to 2 V, 2 V to 0 V, 0 V to −1 V, and −1 V to 0 V, with a ramping step of ±0.02 V. For the retention test, a 0.01 V voltage pulse was applied periodically (3 s interval) to read the device currents. Before testing, a positive voltage sweep (from 0 V to 2 V and 2 V to 0 V) was applied to set the device to LRS, while a negative voltage sweep (0 V to −1 V and −1 V to 0 V) was applied to reset the device to HRS, respectively. The endurance performance of the Co–BTA memristor was evaluated by repeatedly applying a voltage pulse train, with the pulse amplitude changing from 0 V to 2 V, 2 V to 0 V, 0 V to −1 V, and −1 V to 0 V in a ±0.02 V ramping step and a 0.04 s pulse period, respectively, to consecutively program the device's conductance or resistance states between HRS and LRS in an analog manner. The device resistance was simply read as the quotient of the as-read device current divided by the programming voltage. A voltage pulse, with the pulse period of 150 ns (including pulse width of 140 ns and pulse interval time of 10 ns) and an amplitude of 1.5 V, is applied to the device to assess the transformation speed. The energy consumption can be calculated from:

$$E = \int_0^t V_t^2 G_t \mathrm{d}t \quad (1)$$

where E is the energy consumption, and V_t is the voltage applied onto the device at time t while G_t is the device conductance recorded at time t.

DFT simulation of Co–BTA

The theoretical methodology employed in this study utilizes density-functional theory (DFT) with the Vienna *Ab initio* Simulation Package (VASP) software. The generalized gradient approximation-Perdew–Burke–Ernzerhof (GGA-PBE) exchange–correlation functional was used, with *k*-point sampling at the Gamma point. The wave function truncation energy was set to 500 eV and a Gaussian broadening with a width of 0.05 eV was applied. Before static self-consistent calculations, all initial structures underwent a structure optimization using the GGA-PBE function.

BLS implementation for emotion recognition

The BLS was used to realize affective computing for human–machine interaction *via* a Co–BTA-based organic memristor network. The original EEG signals are from the publicly available DEAP dataset.[51] Firstly, a bandpass filter (4–45 Hz) coupled with independent component analysis was used to eliminate ocular artifacts and high-frequency noise. Subsequently, Butterworth bandpass filters decomposed the preprocessed data into four distinct frequency bands (theta (θ) (4–8 Hz), alpha (α) (8–12 Hz), beta (β) (12–30 Hz), and gamma (γ) (30–45 Hz)), which are closely linked to emotional activities. Lastly, the differential entropy (DE) features from each trial were captured using non-overlapping 1-second time windows to capture emotional cues. The DE features were derived from a continuous random variable X with a probability density function $f(x)$ and a defined support set S, as described below:

$$h(X) = -\int_S f(x)\log(f(x))\mathrm{d}x \quad (2)$$

The DE features of emotional states by traditional strategies are still susceptible to historical affective expressions. To tackle this challenge, we introduced a novel module called dynamic entropy feature smoothing (DEFS) to effectively smooth the DE features and uncover their temporal characteristics. DEFS is a dynamic approach that smooths out short-term variations and highlights long-term patterns in EEG signals, facilitating it to track the temporal dynamics of emotional information. The use of DEFS enables better capture of common EEG patterns to distinguish binary emotion levels on the valence and arousal emotional dimensions, respectively. Let $X_{\mathrm{DE}}(i)$ denote the DE feature value at time step i of each trial with delay d, so the smoothed features can be expressed as follows:

$$\bar{X}_{\mathrm{DE}}(n) = \frac{1}{d}[X_{\mathrm{DE}}(n) + X_{\mathrm{DE}}(n-1)\ldots + X_{\mathrm{DE}}(n-d+1)] \quad (3)$$

The instances that underwent DEFS were fed into the BLS for training. To enhance the model's generalization performance and robustness, the final recognition performance was confirmed by averaging the accuracies obtained from 10-fold cross-validation experiments on both the valence and arousal emotional dimensions. The used number of feature nodes is 100 with 10 batches for feature nodes. The number of enhancement nodes is 100, and the sigmoid transfer function with a shrinkage factor of 0.9 for establishment. The weights randomly generated are drawn from the normal distribution on the interval [−1, 1], and the regularization parameter of ridge regression is 0.001.

Author contributions

B. Guo, Z. Yu, and G. Liu conceived the idea. B. Guo, Z. He, S. Liu, B. Zhang, Q. Chen and H. He synthesized and characterized the polymer. B. Guo, S. Liu, Y. Guo, W. Chen, and H. Duan fabricated the memristor devices and conducted the electrical measurements. X. Zhong, B. Guo and J. Zeng performed the time dependent neural network. B. Guo, and Z. Yu analyzed data and visualized it. B. Guo, Z. Yu, X. Zhong, Y. Chen and G. Liu co-wrote the paper. All the authors discussed the results and commented on the manuscript.

Data availability

The authors confirm that the data supporting the findings of this study are available within the article and in the ESI.†

Conflicts of interest

There are no conflicts to declare.

Acknowledgements

This work is supported by the National Key R&D Program of China (2022YFB4700102) and the National Natural Science Foundation of China (61974090 and 62111540271).

Notes and references

1 S. Kumar, *J. Enterp. Inf. Manag.*, 2021, **34**, 1551.
2 R. Picard, *Int. J. Hum-Comput. St.*, 2003, **59**, 55.
3 Siddharth, T. Jung and T. Sejnowski, *IEEE Trans. Affective. Comput.*, 2022, **13**, 96.
4 S. Kumar, N. Sampathila and T. Tanmay, *Meas.: Sens.*, 2022, **24**, 100554.
5 Z. Yu, W. Ying, D. Pravarthana, Y. Li, G. Mao, Y. Liu, C. Hu, W. Zhang, P. He, Z. Zhong, S. Qu, R. Zhang, J. Shang, J. Zhu and R. Li, *Mater. Today Phys.*, 2020, **14**, 100219.
6 Z. Yu, J. Shang, X. Niu, Y. Liu, G. Liu, P. Dhanapal, Y. Zheng, H. Yang, Y. Wu, Y. Zhou, Y. Wang, D. Tang and R. Li, *Adv. Electron. Mater.*, 2018, **4**, 1800137.
7 S. Poria, E. Cambria, R. Bajpai and A. Hussain, *Inf. Fusion*, 2017, **37**, 98.
8 M. Radeta and M. Maiocchi, *2013 Humaine Association Conference on Affective Computing and Intelligent Interaction (ACII)*, 2013, 695.
9 W. Wei, Q. Jia and G. Chen, *2016 IEEE 11th Conference on Industrial Electronics and Applications (ICIEA)*, 2016, 161.
10 G. Zhang, M. Yu, Y. Liu, G. Zhao, D. Zhang and W. Zheng, *IEEE Trans. Affective Comput.*, 2023, **14**, 537.
11 Z. Dong, X. Ji, C. Lai and D. Qi, *IEEE Commun. Mag.*, 2023, **61**, 74.
12 C. Du, F. Cai, M. Zidan, W. Ma, S. Lee and W. Lu, *Nat. Commun.*, 2017, **8**, 2204.
13 L. Sun, Z. Wang, J. Jiang, Y. Kim, B. Joo, S. Zheng, S. Lee, W. Yu, B. Kon and H. Yang, *Sci. Adv.*, 2021, **7**, eabg1455.
14 J. Zhu, X. Zhang, R. Wang, M. Wang, P. Chen, L. Cheng, Z. Wu, Y. Wang, Q. Liu and M. Liu, *Adv. Mater.*, 2022, **34**, 2200481.
15 X. Yi, Z. Yu, X. Niu, J. Shang, G. Mao, T. Yin, H. Yang, W. Xue, P. Dhanapal, S. Qu, G. Liu and R. Li, *Adv. Electron. Mater.*, 2019, **5**, 1800655.
16 Z. Yu, Y. Mao, Z. Wu, F. Li, J. Cao, Y. Zheng, X. Zhong, L. Wang, J. Zhu, P. Gao, W. Ying and G. Liu, *Adv. Funct. Mater.*, 2023, 2307503.
17 S. Liu, Z. He, B. Zhang, X. Zhong, B. Guo, W. Chen, H. Duan, Y. Tong, H. He, Y. Chen and G. Liu, *Adv. Sci.*, 2023, 2305075.
18 B. Zhang, W. Chen, J. Zeng, F. Fan, J. Gu, X. Chen, L. Yan, G. Xie, S. Liu, Q. Yan, S. Baik, Z. Zhang, W. Chen, J. Hou, M. El–Khouly, Z. Zhang, G. Liu and Y. Chen, *Nat. Commun.*, 2021, **12**, 1984.
19 B. Zhang, F. Fan, H. Xue, G. Liu, Y. Fu, X. Zhuang, X. Xu, J. Gu, R. Li and Y. Chen, *Nat. Commun.*, 2019, **10**, 736.
20 F. Shu, X. Chen, Z. Yu, P. Gao and G. Liu, *Molecules*, 2022, **27**, 8888.
21 Y. Ni, L. Lin, Y. Shang, L. Luo, L. Wang, Y. Lu, Y. Li, Z. Yan, K. Zhang, F. Cheng and J. Chen, *Angew. Chem., Int. Ed.*, 2021, **60**, 16937.
22 Y. Chen, M. Tang, Y. Wu, X. Su, X. Li, S. Xu, S. Zhuo, J. Ma, D. Yuan, C. Wang and W. Hu, *Angew. Chem., Int. Ed.*, 2019, **58**, 14731.
23 P. Saha, M. Sahad, S. Sathyanarayana and B. Das, *ACS Nano*, 2024, **18**, 1.
24 A. Thomas, P. Saha, M. Sahad, N. Krishnan and B. Das, *ACS Appl. Mater. Interfaces*, 2024, **16**, 16.
25 H. Kim, D. Woo, S. Jin, H. Kwon, K. Kwon, D. Kim, D. Park, D. Kim, H. Jin, H. Choi, T. Shim and J. Park, *Adv. Mater.*, 2022, **34**, 2203643.
26 J. Oh, S. Kim, C. Lee, J. Cha, S. Yang, S. Im, C. Park, B. Jang and S. Choi, *Adv. Mater.*, 2023, **35**, 2300023.
27 B. Tossoun, D. Liang, S. Cheung, Z. Fang, X. Sheng, J. Strachan and R. Beausoleil, *Nat. Commun.*, 2024, **15**, 551.
28 D. Chen, X. Zhi, Y. Xia, S. Li, B. Xi, C. Zhao and X. Wang, *Small*, 2023, **19**, 2301196.
29 X. Li, L. Zhang, R. Guo, J. Chen and X. Yan, *Adv. Mater. Technol.*, 2020, **5**, 2000191.
30 S. Sinha, M. Sahad, R. Mondal, S. Das, L. Manamel, P. Brandao, B. Bruin, B. Das and N. Paul, *J. Am. Chem. Soc.*, 2022, **144**, 20442.
31 J. Kim, B. Cho, K. Kim, T. Lee and G. Jung, *Adv. Mater.*, 2011, **23**, 2104.
32 S. Song, B. Cho, T. Kim, Y. Ji, M. Jo, G. Wang, M. Choe, Y. Kahng, H. Hwang and T. Lee, *Adv. Mater.*, 2010, **22**, 5048.
33 T. Dao, *IEEE 2014 International Conference on Advanced Technologies for Communications (ATC)*, 2014, 32.
34 Y. Xu, H. Wang, D. Ye, R. Yang, Y. Huang and X. Miao, *IEEE Electron Device Lett.*, 2022, **43**, 116.
35 C. Wu, T. Kim, H. Choi, D. Strukov and J. Yang, *Nat. Commun.*, 2017, **8**, 752.
36 H. Park, M. Kim, H. Kim and S. Lee, *Adv. Electron. Mater.*, 2021, **7**, 2100299.

37 B. Cho, T. Kim, M. Choe, G. Wang, S. Song and T. Lee, *Org. Electron.*, 2009, **10**, 473.
38 J. Kim, B. Cho, K. Kim, T. Lee and G. Jung, *Adv. Mater.*, 2011, **23**, 2104.
39 S. Song, B. Cho, T. Kim, Y. Ji, M. Jo, G. Wang, M. Choe, Y. Kahng, H. Hwang and T. Lee, *Adv. Mater.*, 2010, **22**, 5048.
40 B. Cho, K. Nam, S. Song, Y. Ji, G. Jung and T. Lee, *Curr. Appl. Phys.*, 2012, **12**, 940.
41 Y. Ji, A. Cha, S. Lee, S. Bae, S. Lee, D. Lee, H. Choi, G. Wang and T. Kim, *Org. Electron.*, 2016, **29**, 66.
42 Y. Ji, D. Zeigler, D. Lee, H. Choi, A. Jen, H. Ko and T. Kim, *Nat. Commun.*, 2013, **4**, 2707.
43 T. Kim, D. Zeigler, O. Acton, H. Yip, H. Ma and A. Jen, *Adv. Mater.*, 2012, **24**, 828.
44 B. Cho, J. Yun, S. Song, Y. Ji, D. Kim and T. Lee, *Adv. Funct. Mater.*, 2011, **21**, 3976.
45 Y. Song, J. Jang, D. Yoo, S. Jung, S. Hong, J. Lee and T. Lee, *Org. Electron.*, 2015, **17**, 192.
46 R. Huang, Y. Tang, Y. Kuang, W. Ding, L. Zhang and Y. Wang, *IEEE Trans. Electron Devices*, 2012, **59**, 3578.
47 T. Chen, J. Dou, L. Yang, C. Sun, N. Libretto, G. Skorupskii, J. Miller and M. Dinca, *J. Am. Chem. Soc.*, 2020, **142**, 28.
48 D. Kuzum, S. Yu and H. Wong, *Nanotechnology*, 2013, **22**, 382001.
49 X. Wang, T. Zhang, X. Xu, L. Chen, X. Xing and L. Chen, *2018 IEEE International Conference on Bioinformatics and Biomedicine (BIBM)*, 2018, 1240.
50 T. Zhang, X. Wang, X. Xu and C. Chen, *IEEE Trans. Affective. Comput.*, 2022, **13**, 379.
51 S. Koelstra, C. Muehl, M. Soleymani, J. Lee, A. Yazdani, T. Ebrahimi, T. Pun, A. Nijholt and I. Patras, *IEEE Trans. Affective. Comput.*, 2012, **3**, 1.